Inorganic Chemistry

Article

pubs.acs.org/IC

Diversity of Microstructural Phenomena in Superconducting and Non-superconducting $Rb_xFe_{2-y}Se_2$: A Transmission Electron Microscopy Study at the Atomic Scale

Maria V. Roslova,[†,‡,§] Oleg I. Lebedev,[‡] Igor V. Morozov,[†,§] Saicharan Aswartham,[§] Sabine Wurmehl,[§,∥] Bernd Büchner,[§,∥] and Andrei V. Shevelkov*[,†]

[†]Department of Chemistry, Lomonosov Moscow State University, 119991 Moscow, Russia

[‡]Laboratoire CRISMAT, UMR 6508, CNRS-ENSICAEN, 14050 Caen, France

[§]Leibniz Institute for Solid State and Materials Research, IFW-Dresden, D-01171 Dresden, Germany

[∥]Institut für Festkörperphysik, Technische Universität Dresden, D-01062 Dresden, Germany

ABSTRACT: Superconducting (SC) and non-superconducting (non-SC) $Rb_xFe_{2-y}Se_2$ crystals were grown using the "self-flux" technique in order to assign the microstructural changes to the onset of superconductivity in complex iron selenides. The crystals were thoroughly characterized by magnetic susceptibility and transport measurements as well as powder X-ray diffraction. Special attention was paid to the comparison of the microstructure of the crystals with and without the superconducting transition by means of transmission electron microscopy (TEM). It is shown that the alternation of ordered and disordered regions on the sample surface and along the *c*-axis is characteristic for both SC and non-SC materials and therefore does not necessarily represent a trigger of superconductivity. Three types of electron diffraction patterns were found for the superconducting $Rb_xFe_{2-y}Se_2$ sample, of which one is observed for the first time and originates from alkali metal ordering. Moreover, for the superconducting $Rb_xFe_{2-y}Se_2$ material a monoclinic distortion with $\beta \sim 87°$ was observed, leading to the space group $I2/m$. This monoclinic distortion seems to be an attribute of the superconducting material only, whereas in the non-superconducting sample the orthogonality of the crystallographic axes is preserved.

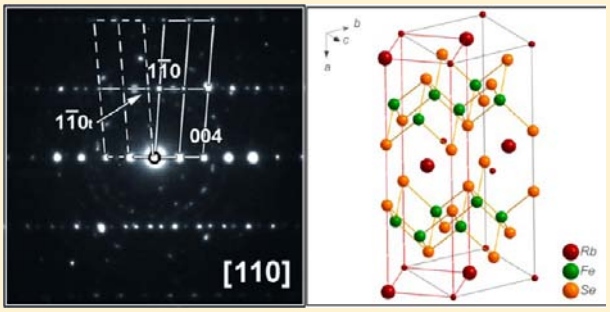

I. INTRODUCTION

The recently discovered $A_xFe_{2-y}Se_2$ (A = K, Rb, Cs) superconductors exhibit several unique characteristics which are not observed in other iron-based superconducting materials.[1] A complex multiphase nature of these compounds complicates understanding of the mechanisms responsible for high-temperature superconductivity. The composition of these compounds in most cases deviates from the ideal 122 stoichiometry owing to the appearance of vacancies in the crystal structure.[2] At least five different types of iron ordering have been found in $A_xFe_{2-y}Se_2$ compounds using such techniques as X-ray[3,4] and neutron diffraction[5−9] as well as high-resolution microscopy techniques including transmission electron (TEM)[10−13] and scanning tunneling (STM) microscopies.[14,15] To date, it is well-known that the main phase in $A_xFe_{2-y}Se_2$ has the $I4/m$ symmetry with a regular distribution of iron vacancies that leads to a $\sqrt{5} \times \sqrt{5}$ superstructure of the $ThCr_2Si_2$ structure type subcell; this main phase remains magnetically ordered up to 520 K[2] and transforms at high temperatures to the $I4/mmm$ disordered phase with no magnetic order.[8] The presence of a second phase was noted in many diffraction studies and often referred to as a $\sqrt{2} \times \sqrt{2}$ superstructure; moreover, neutron[16,17] and X-ray synchrotron radiation diffraction studies[18−20] of superconducting $A_xFe_{2-y}Se_2$ samples provide evidence for the chemical phase separation between these two phases. The two-phase nature of $A_xFe_{2-y}Se_2$ samples was confirmed by TEM,[10,12] STM,[14] NMR,[21,22] muon-spin relaxation,[22,23] Mössbauer spectroscopy,[24,25] and high-resolution electron backscatter diffraction (HR-EBSD)[26,27] techniques. The secondary phase is compressed in the tetragonal *ab*-plane and expanded along the *c*-direction according to the literature.[28] However, the nature of this phase is still a matter of speculations. It is argued[28] that the symmetry of the second phase should be not higher than monoclinic due to the 4-fold splitting of *00l* reflections with high *l* values in the *ab*-plane, with a monoclinic angle being 90.7°. However, other authors[6] described the second phase in the orthorhombic symmetry (space group *Pmna*) using a vacancy ordered model. Recent neutron powder diffraction[29] and high-resolution synchrotron powder diffraction[20] investigations reveal the existence of a vacancy disordered structure with the composition close to $A_\delta Fe_2Se_2$ ($\delta \sim 0.3$−0.6) and the

Received: October 28, 2013
Published: November 27, 2013

   dx.doi.org/10.1021/ic402710r | *Inorg. Chem.* 2013, 52, 14419−14427

*I*4/*mmm* space group in the superconducting $A_xFe_{2-y}Se_2$ samples.

The intrinsically two-phase nature of the SC samples is manifested by the inhomogeneous morphology observed as a network-like pattern of alternating bright and dark stripes on the sample surface. Thus, by means of SEM and EBSD[27] the alignment of the stripes in the $K_xFe_{2-y}Se_2$ crystal is along the [110] directions of the matrix, as it was also measured on $Cs_xFe_{2-y}Se_2$.[26] The element distribution maps showed that the platelets are depleted in K and enriched in Fe, whereas the matrix composition is close to $K_2Fe_4Se_5$. An STM investigation[30] suggests that the phase with the $K_{0.5}Fe_{1.75}Se_2$ composition comprising a single Fe vacancy for every eight Fe sites leading to a $\sqrt{8} \times \sqrt{10}$ parallelogram arrangement might play an important role in the onset of superconductivity in the $K_xFe_{2-y}Se_2$ samples. These findings call for further investigations of the A−Fe-Se systems with low alkali metal content. However, the interpretation of results requires careful structure characterization at the atomic level.

This Article is devoted to a detailed investigation of the microstructure of superconducting and non-superconducting $Rb_xFe_{2-y}Se_2$ crystals with a different nominal Rb content. $Rb_xFe_{2-y}Se_2$ crystals were characterized by means of the X-ray powder diffraction, magnetic susceptibility, and transport measurements, and by transmission electron microscopy. Special attention was paid to the comparison of the microstructure of samples with and without superconducting transition. In particular, we present evidence that Rb ordering appears to be a prerequisite for the superconductivity. While bulk powder X-ray diffraction cannot give a decisive answer on the nature of the superconducting phase, local methods such as TEM enabled us to find different superstructure patterns for the superconducting and non-superconducting phases. We find that a monoclinic distortion observed in our study seems to be an attribute of the superconducting material, whereas in the non-superconducting sample the orthogonality of crystallographic axes is preserved.

II. EXPERIMENTAL SECTION

1. Synthesis and Crystal Growth. Single crystals of $Rb_xFe_{2-y}Se_2$ were grown by the self-flux method.[31,32] All preparation steps were performed in an argon-filled glovebox with O_2 and H_2O content less than 0.1 ppm. Starting FeSe was obtained by reacting Fe powder (99.998%, Puratronic) with Se powder (99.999%, Chempur) in a ratio of Fe:Se = 1:0.98 at 780 °C for 72 h. For the crystal growth we used the prereacted FeSe powder and Rb pieces in varying molar ratios. For the preparation of the superconducting sample further denoted as sample 1, the reaction mixture was put into an alumina crucible inside a small quartz tube. The small quartz tube was sealed under high vacuum and was put in a larger quartz tube which was subsequently evacuated and sealed. The tube was heated to 1050 °C in 7 h, kept at this temperature for 3 h, and slowly cooled to 750 °C with a rate of 6 deg·h^{-1}, followed by air-quenching.

For the preparation of the non-superconducting sample with a lower nominal Rb content, denoted further as sample 2, the precursor materials were placed in an alumina crucible inside a niobium container which was welded under 1 atm of Ar in an arc-melting facility. The niobium container was sealed in an evacuated quartz tube and heated to 1080 °C, kept at this point for 3 h, and cooled to 750 °C with a rate of 6 deg·h^{-1}. The sample was quenched in air similarly to the previous case. It should be noted that all attempts to prepare a superconducting sample in the Nb container have failed so far. However, the use of welded crucibles allows one to prevent possible losses of the volatile alkali metal, which is crucial for growing crystals from Rb-poor starting compositions.

Thin plate-like single crystals with a shiny bronze surface were extracted mechanically from the ingot. All crystals grow in a layered morphology; they are easily cleaved along the *ab*-plane.

2. Experimental Details. The microstructure and average composition of the $Rb_xFe_{2-y}Se_2$ crystals were investigated by scanning electron microscopy (SEM) using a XL30 Philipps IN400 microscope equipped with an electron microprobe analyzer for the semi-quantitative elemental analysis in the energy dispersive X-ray spectroscopy (EDX) mode. SEM images were taken at 15 kV in the backscattered electron (BSE) mode. The concentrations of the elements in the samples were measured on a freshly cleaved surface with a minimal exposure to air to prevent their oxidation. The composition was determined by examination of 7−10 points on a crystal surface for several crystals of each batch and concomitant averaging.

Powder X-ray diffraction patterns for phase analysis were recorded using a Rigaku Miniflex diffractometer with Cu $K\alpha_{1+2}$ radiation in the reflection mode. The structural characterization of superconducting and non-superconducting samples 1 and 2 was performed by X-ray diffraction measurements in a $\theta-2\theta$ Bragg−Brentano geometry on a Rigaku D/MAX 2500 diffractometer with rotating anode (Cu $K\alpha_1$ radiation, graphite monochromator). The unit cell parameters were determined and refined with WinXpow[33] and Jana2006[34] software packages.

The magnetization was measured using a superconducting quantum interference magnetometer SQUID-5T "Quantum Design" in a temperature range of 5−300 K at H = 20 Oe and 1 T applied parallel and perpendicular to the *ab*-plane of a crystal after zero-field cooling.

The resistivity measurements were done on the PPMS-9T "Quantum Design" for a rectangular sample in a temperature range of 5−250 K using a standard four-probe DC technique. The crystal was 3.05 mm in length (1.05 mm distance between potential contacts) and 2.97 mm in width and had a thickness of 0.25 mm. The Ag wires were attached to the crystal with a conductive silver paste.

Electron diffraction (ED) patterns and high-resolution transmission electron microscopy (HRTEM) images were recorded on a FEI Tecnai-G2 microscope operating at 300 keV and having 0.17 nm point resolution. Samples for TEM experiments were obtained by grinding the crystals in an agate mortar in an Ar atmosphere to prevent their oxidation. The powder was suspended in anhydrous *n*-hexane or *n*-butanol and deposited on a holey carbon grid. It is worthwhile to note that due to their anisotropic layered nature the crystals exhibit preferred orientation; therefore, transverse sections (along the *ab*-plane) can be readily obtained in the TEM experiment rather than axial ones (along the *c*-axis) due to goniometer tilting limitation.

The HRTEM images and ED patterns were simulated using the MacTempas and Crystal Kit software. For the basic structure simulation, different specimen thicknesses (t) in the range from 0.20 to 1.20 nm and defocus values (Δf) in the range from −10 to −60 nm were usually assumed. The calculated images were compared with the experimental observed HRTEM images.

III. RESULTS AND DISCUSSION

1. Comments to the Synthesis. In the course of the synthetic research a series of samples in the Rb−Fe−Se system was obtained by varying the nominal composition of the starting mixture. Detailed investigations of these samples showed a tremendous difference in the composition and microstructure of the crystals. The systematic exploration of the compositional space allowed us to find a narrow range of elemental ratios in the starting mixtures required for the preparation of the phases with desired stoichiometry. Two different types of the synthetic setup were used mainly because the product compositions are controlled by a subtle interplay of kinetic and thermodynamic factors, including the cooling rate, the internal pressure inside the ampule, and the initial ratio of the reagents. Each synthesis resulted in a sample consisting of

dx.doi.org/10.1021/ic402710r | *Inorg. Chem.* 2013, 52, 14419−14427

shiny-bronze layered crystals grown on top of a batch that consisted mainly of unreacted t-FeSe and reduced α-Fe. Although samples 1 and 2 presented in this work possess a microinhomogeneity (see below), their compositional variations are limited within a definite region and seem to be an intrinsic property of both superconducting and non-superconducting samples. Outside this empirically found microinhomogeneity range a variety of compounds such as the Fe vacancy ordered $Rb_2Fe_4Se_5$ phase, the tetragonal modification of $FeSe_{1-\delta}$, or even the $RbFe_2Se_3$ phase ($CsCu_2Cl_3$ structure type, space group *Cmcm*[35]) can be prepared as side products or major phases.

The starting compositions and those obtained by means of the EDX analysis are summarized in Table 1 together with the results of the X-ray powder diffraction analysis for samples 1 and 2 under investigation.

Table 1. Preparation Conditions and EDX and XRD Data for $Rb_xFe_{2-y}Se_2$ Samples

		EDX data			lattice params	
no.	starting element ratio Rb:Fe:Se	Rb	Fe	Se	*a*, Å	*c*, Å
1	0.8:2:1.96	0.73(3)	1.72(4)	2.00	3.903(6)	14.698(5)
2	0.5:2:1.96	0.75(1)	1.66(4)	2.00	3.926(7)	14.528(3)

2. Morphology. Figure 1 shows typical SEM images of freshly cleaved surfaces perpendicular to the *c*-axis for samples 1

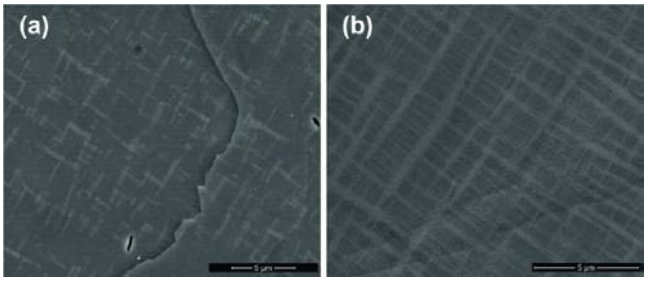

Figure 1. Scanning electron micrographs taken at 15 keV in the BSE mode showing the morphology of $Rb_xFe_{2-y}Se_2$ crystals in the *ab*-plane: (a) SC sample 1; (b) non-SC sample 2.

and 2. It can be clearly seen that both samples are actually two-phase in nature and consist of alternating dark and light stripes, each 50−200 nm thick. In addition to the terrace steps arising from the growth of the crystals in layered morphology, square arrays of dark features with linear cross-section can be clearly seen for all crystals. According to the literature,[26,36] these typical linear cross-sections are aligned along the crystallographic [110] directions. Nevertheless, the appearance of the dark and light stripes is significantly less pronounced in the superconducting sample 1 than in the non-superconducting sample 2, leading to the observations of brighter islands within the dark matrix in sample 1 and fully separated dark areas surrounded by bright areas in sample 2. The phase contrast in the electron images indicates that the minor phase is compositionally different from the matrix. It should be noted that the insufficient spatial resolution of the EDX method does not allow an unambiguous determination of elemental ratios in these phases; therefore, an averaged composition over the crystal surface will be referred to in the following discussion.

These features in the microstructure of the samples 1 and 2 call for further careful structure investigations by X-ray powder diffraction and TEM as well as magnetic susceptibility and transport measurements to relate those differences to the physical macroscopic properties.

3. X-ray Powder Diffraction. The complexity of the diffraction patterns recorded with a conventional X-ray diffractometer makes it possible to index unambiguously only the reflections belonging to the parent $ThCr_2Si_2$-type cell with the *I*4/*mmm* space group. The corresponding lattice parameters of the investigated samples are given in Table 1. Apparently, there is a correlation between the *a*- and *c*-parameters for the superconducting and non-superconducting samples. Thus, the *a*-parameter of the unit cell for the superconducting sample is lower than for the non-superconducting one, whereas the trend for the *c*-parameter is opposite. This observation is in agreement with the literature data,[6,27] stating that the superconducting phase is compressed in the tetragonal *ab*-plane and expanded along the *c*-direction. Although a definite relationship between the unit cell parameters and the stoichiometry of $Rb_xFe_{2-y}Se_2$ compounds has not been found, we can argue that the observed ratio between the *c*- and *a*-parameters in a sample may indicate the onset of superconductivity. At the same time it should be also kept in mind that the changes of the lattice parameters in the case of $Rb_xFe_{2-y}Se_2$ compounds cannot be described by a one-parameter function, e.g., the content of alkali metal vs cell volume, but are influenced by many yet uncontrolled factors.

X-ray powder diffraction patterns recorded with a diffractometer with a better signal-to-noise ratio for samples 1 (red crosses) and 2 (black crosses) are given in Figure 2. The

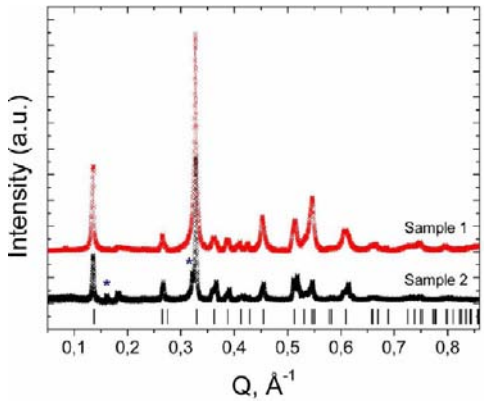

Figure 2. X-ray diffraction patterns of SC (sample 1) and non-SC (sample 2) $Rb_xFe_{2-y}Se_2$ crystals. Crosses are the experimental data; ticks denote positions of Bragg reflections for the parent $ThCr_2Si_2$ subcell with the *I*4/*mmm* space group.

interpretation of the XRD data is complicated by the fact that the intrinsic multiphase nature of the compounds and their relatively low crystallinity lead to a significant broadening of the Bragg peaks, especially in the case of the superconducting sample 1. Careful inspection of this pattern revealed the presence of the superstructure reflections of the Fe vacancy ordered $Rb_2Fe_4Se_5$ phase with the space group *I*4/*m* and the lattice parameters $a = b = 8.728(2)$ Å and $c = 14.698(4)$ Å. In the low-angle range of the XRD profile one can observe the reflections which can be well-described by an I-centered

dx.doi.org/10.1021/ic402710r | *Inorg. Chem.* 2013, 52, 14419−14427

orthorhombic supercell with the lattice parameters a = 5.441(1) Å, b = 10.929(2) Å, and c = 14.801(2) Å.

In the profile of the non-superconducting sample some fairly intensive reflections forbidden for the I-centered cell are clearly seen. These additional reflections can be indexed in a unit cell with the tetragonal metric symmetry and the lattice constants $a = b$ = 5.515(2) Å and c = 14.528 (4) Å. The actual symmetry of this phase was found to be orthorhombic according to the electron diffraction data (see text that follows). Besides, there are also two small peaks, marked by asterisks, belonging to the impurity $FeSe_{1-\delta}$ phase (space group $P4/nmm$).[37]

4. Magnetic Susceptibility Measurements. Figure 3a shows magnetic susceptibility as a function of temperature

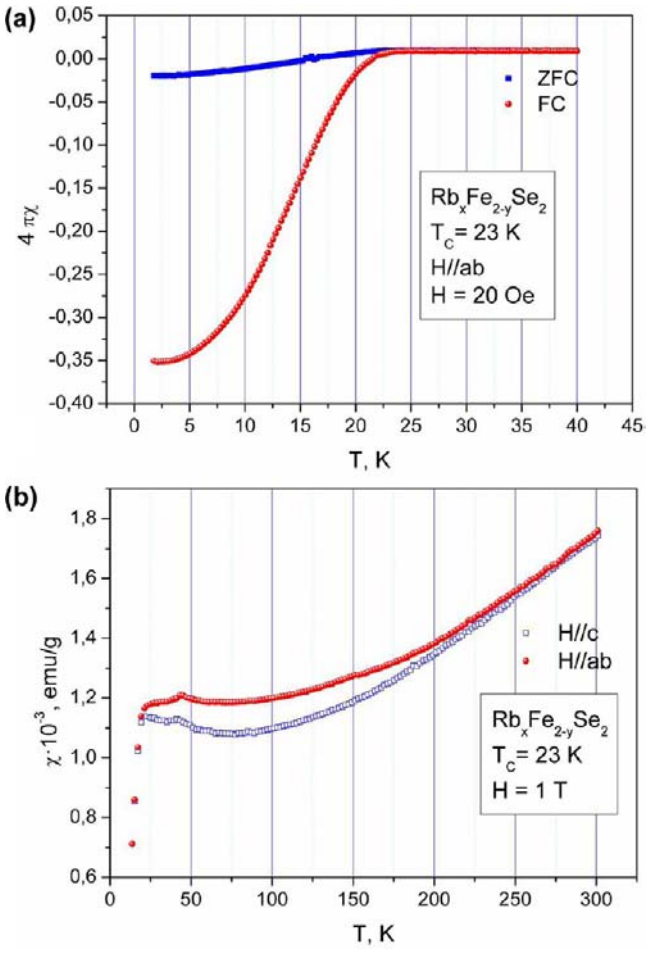

Figure 3. (a) Temperature dependence of the ZFC and FC susceptibility taken at 20 Oe with the magnetic field applied parallel to the *ab*-plane for SC sample 1; (b) magnetic susceptibility at 1 T for SC sample 1 with the magnetic field applied along and perpendicular to the *c*-axis.

below 40 K for the superconducting $Rb_{0.73(6)}Fe_{1.72(4)}Se_2$ single crystalline sample (T_C = 23.6 K) under a magnetic field of 20 Oe applied parallel to the *ab*-plane using field-cooled (FC) and zero-field-cooled (ZFC) conditions. The magnitude of the diamagnetic signal indicates that the Meissner screening at H = 20 Oe is about 35%, but it should be noted that this value may not be proportional to the superconducting volume fraction in the sample.[38] The ZFC magnetic susceptibility becomes saturated below 4 K. The width of the transition is about 20 K which might originate from an intrinsic inhomogeneity of the sample. Figure 3b shows the magnetic susceptibility of the superconducting sample with the magnetic field of 1 T applied parallel and perpendicular to the *c*-axis in the temperature range from 10 to 300 K. At high temperatures, both magnetization curves lay basically on top of each other, but they start to split at around 190 K. This temperature coincides with the maximum in resistivity (see below) and marks the onset of the Fe vacancies ordering.[38] The ratio between $\chi_\perp$ and $\chi_\parallel$ in addition to the similar weak temperature dependence might be characteristic for an anisotropic antiferromagnet, which additionally confirms the predominance of the Fe vacancy ordered $Rb_2Fe_4Se_5$ phase in the superconducting sample.[31]

5. Transport Properties Measurements. Figure 4a shows the in-plane resistivity as a function of temperature for the

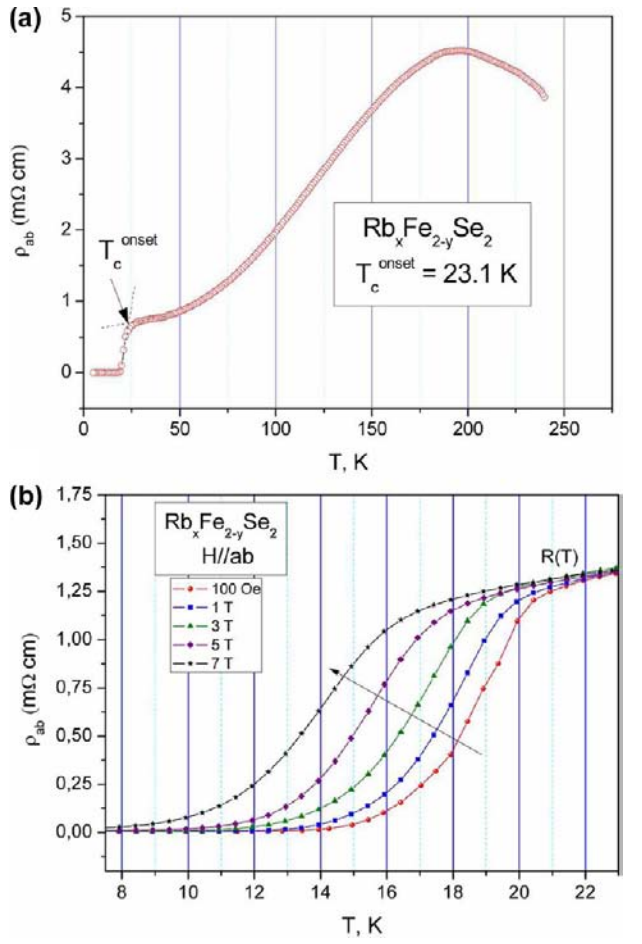

Figure 4. (a) Temperature dependence of resistivity for SC sample 1 with the magnetic field applied parallel to the *ab*-plane. (b) Resistivity as a function of temperature for SC sample 1 under the magnetic field up to 7 T applied in the *ab*-plane. The inset shows the temperature dependence of upper critical field $H_{c2}(T)$ for SC sample 1.

superconducting sample 1. Sample 1 exhibits semiconductor-like behavior at high temperature, followed by maximum resistivity at about 190 K, metallic behavior below 190 K, and a superconducting transition at about 23 K. Similar resistivity behavior of $A_xFe_{2-y}Se_2$ (A = K, Rb, Cs, K/Tl) compounds was reported previously.[39,40] Note that the resistivity of the $Rb_{0.73(6)}Fe_{1.72(4)}Se_2$ single crystal is 4.5 mOhm·cm at 230 K, which is much larger than for the majority of iron pnictide superconductors due to the isolating behavior of the respective selenides in contrast to the metallic properties of the

dx.doi.org/10.1021/ic402710r | Inorg. Chem. 2013, 52, 14419−14427

pnictides.[41−44] Resistivity as a function of temperature under the magnetic field up to 7 T applied in the *ab*-plane is given in Figure 4b. The measurements were performed on cooling after heating in zero field. The inset in Figure 4b shows the temperature dependence of the upper critical field $H_{c2}(T)$ estimated using the criterion of the 90% drop of the normal state resistivity. The $H_{c2}(0K)$ value can be calculated using the one-band Werthamer−Helfand−Hohenberg formula,[45] $H_{c2}(0K) = -0.693T_C[dH_{c2}/dT]T_C$, where $[dH_{c2}/dT]T_C$ is obtained from the slope of the H_{c2} versus T curve at T_C. The estimation gives a value of 20 T for the in-plane configuration, which is comparable with the values previously reported for other $A_xFe_{2-y}Se_2$ compounds.[40]

Sample 2 is a non-superconducting sample, demonstrating the semiconductor-like behavior in the whole temperature range (not shown). Thus, the samples under consideration (samples 1 and 2) have similar compositions and morphology but different unit cell parameters and physical properties, suggesting that some delicate structural peculiarities may result in significantly different physical macroscopic properties of these compounds.

6. Electron Diffraction Patterns. TEM observations on the microstructure features in the Rb−Fe−Se system reveal a rich variety of structural phenomena, such as iron vacancy ordering and phase separation similar to the literature data published on the K−Fe−Se system.[10−15]

A series of ED patterns taken along the relevant zone-axis directions for the SC sample 1 are given in Figures 5 and 6. The

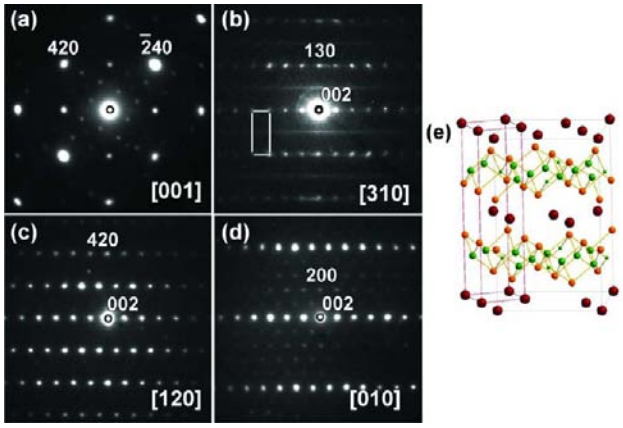

Figure 5. Electron diffraction patterns for SC $Rb_xFe_{2-y}Se_2$ (sample 1) taken along the (a) [001], (b) [310], (c) [120], and (d) [010] zone-axis directions showing the superstructure I reflections. (e) Structural model for superstructure I. The Rb, Fe, and Se atoms are indicated as red, green, and orange circles, respectively. The edges of the original $ThCr_2Si_2$ subcell are drawn in red color. The relative diameter of the spheres represents the occupancy of the respective positions.

brightest spots correspond to the basic tetragonal body-centered $ThCr_2Si_2$-type subcell with $a_s = b_s \approx 3.9$ Å and $c_s \approx 14.5$ Å. It should be stressed that the ED data yield the same results as those of powder XRD. The weaker spots correspond to the different supercell reflections. There are at least three sets of superstructure reflections found in Figures 5 and 6.

The first set of superstructure reflections, given in Figure 5a−d, can be indexed in the well-known tetragonal body-centered supercell[3−15] with the unit cell parameters $a_I = b_I = a_s\sqrt{5} \approx 8.7$ Å and $c_I = c_s = 14.5$ Å and the space group $I4/m$, denoted

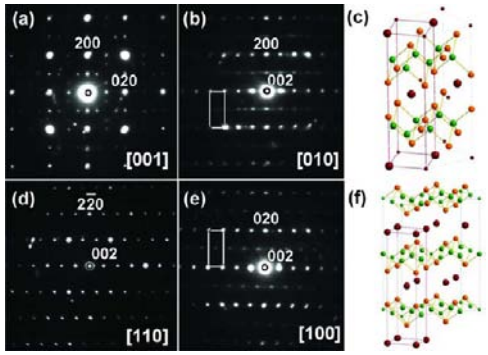

Figure 6. Electron diffraction patterns of SC $Rb_xFe_{2-y}Se_2$ (sample 1) taken along the (a) [001], (b) [010], (d) [110], and (e) [100] zone-axis directions showing the superstructure II and III reflections. (c, f) Structural models for superstructures II and III. The Rb, Fe, and Se atoms are indicated as red, green, and orange circles, respectively. The edges of the original $ThCr_2Si_2$ subcell are drawn in red color. The relative diameter of spheres represents the occupancy of the respective positions.

further as superstructure I. Superstructure I is based on the vectors $a_I = 2a_s + b_s$ and $b_I = -a_s + 2b_s$.

In Figure 6a, a combination of two sets of superstructure reflections along the [001] direction is presented. Each set can be indexed in the orthorhombic symmetry. The unit cells of the superstructures are based on the vectors $a_{II} = a_s + b_s$, $b_{II} = 2(a_s - b_s)$ (superstructure II) and $a_{III} = a_s + b_s$, $b_{III} = a_s - b_s$ (superstructure III) of the parent $ThCr_2Si_2$-type subcell. They have the unit cell parameters $a_{II} = a_s\sqrt{2} \approx 5.5$ Å, $b_{II} = 2a_s\sqrt{2} \approx 11$ Å, $c_{II} = c_s = 14.5$ Å (superstructure II) and $a_{III} = b_{III} = a_s\sqrt{2} \approx 5.5$ Å, $c_{III} = c_s = 14.5$ Å (superstructure III).

For the reciprocal space reconstruction and determination of the space group for each supercell, the ED patterns along the orthorhombic [010], [101], and [100] zone-axis directions were used additionally. Superstructure I exhibits a diffuse streak line at $^1/_2$ [130] distance in its [310] zone (Figure 5b) parallel to the [001] zone-axis direction that certainly indicates the disordering along the *c*-axis. A feature of the ED patterns along the orthorhombic [010] zone-axis direction for superstructures II and III possessing the orthorhombic symmetry is a set of 10*l* spots. The patterns with $l = 2n$ were observed for superstructure II while for superstructure III two types of the patterns with either $l \neq 2n$ or $l = 2n$ were found. To describe superstructure II, we relied on the assumption made in the literature,[13] where it was shown that the symmetry of the Fe vacancy ordering corresponding to superstructure II is not higher than *Ibam*. The reflection condition corresponding to the appearance of the 10*l* spots row with $l \neq 2n$ in the orthorhombic [010] direction (Figure 6d) are satisfied for the space group $I2_22$, which is a maximal subgroup of *Ibam*. A transformation matrix which relates the coordinate system of the $I2_22$ subgroup to that of the *Ibam* supergroup is a unitary transformation with an origin shift (0, 0, $^1/_4$). The symmetry lowering causes a splitting of the 8*g* Fe positions into the 4*g* and 4*h* ones, 4*b* positions into 2*b* and 2*d*, and 4*a* positions into 2*a* and 2*c* positions. Thus, the unit cell with the space group $I2_22$ has the cell parameters $a_{II} = a_s\sqrt{2} \approx 5.5$ Å, $b_{II} = 2a_s\sqrt{2} \approx 11$ Å, and $c_{II} = 14.5$ Å.

For a description of superstructure III we should take into account refs 11 and 13 where the authors suggest that the additional superstructure reflections ($^1/_2$, $^1/_2$, 0) of the original subcell might be caused not by Fe vacancy ordering but rather

dx.doi.org/10.1021/ic402710r | *Inorg. Chem.* 2013, 52, 14419−14427

by alkali metal ordering. Possible subgroups arising from alkali metal ordering were searched using the program ISODISTORT[46] allowing us to generate and explore distortion modes induced by irreducible representations of the parent space group symmetry. Ordering of Rb atoms was chosen as the only distortion parameter, and the search was conducted over all special k-points. The observed reflection conditions may correspond to the space group *Cmmm* generated by the X1+ irreducible representation of the parent *I*4/*mmm* space group. The corresponding unit cell is based on the vectors $a_{III}' = c_s$, $b_{III}' = a_s + b_s$, and $c_{III}' = -a_s + b_s$. In order to preserve the same *c*-axis direction, it is convenient to change to the nonstandard setting *Ammm*. The unit cell with the space group *Ammm* has the cell parameters $a_{III} = b_{III} = a_s\sqrt{2} \approx 5.5$ Å and $c_{III} = 14.5$ Å. The two observed variants of additional spots in the [110] direction of the parent subcell can be now described as 10*l* or 01*l* reflections in the respective [010] and [100] directions of the orthorhombic cell constructed as described above.

Another important feature of sample 1 is the absence of $^1/_2\,^1/_2 l$ reflections in the ED patterns along the [110] zone-axis direction that we assign to the monoclinic distortion. Such a monoclinic distortion can be clearly seen in Figure 7, where the

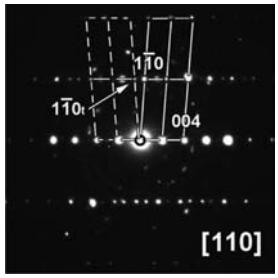

Figure 7. Monoclinic distortion accompanied by the twinning observed in the [110] zone-axis direction for SC $Rb_xFe_{2-y}Se_2$ (sample 1).

angle between the *a* and *c* axes is not exactly 90°. The monoclinic angle was found to be approximately 87°. It is important to note that the monoclinic distortion is accompanied by the twinning observed in the [110] direction with the common (001) twinning plane. Therefore the reflection broadening observed in the powder XRD patterns may be consistent with this monoclinic distortion, and this can be observed directly by electron diffraction. The monoclinically distorted unit cell with the space group *I*2/*m* has the unit cell edges $a_m = b_m \approx 3.9$ Å and $c_m \approx 14.5$ Å. This model can successfully describe the diffraction pattern in the [010] zone-axis direction shown in Figure 7. One can speculate that the coexistence of several related phases within a single crystal may induce a high internal stress leading to the observed monoclinic distortion.

Importantly, the superstructure patterns are strikingly different for samples 1 and 2. For the non-superconducting sample 2 the electron diffraction patterns along the [001], [100], and [110] zone-axis directions are given in Figure 8. The ED pattern along the [001] direction shows bright extra spots 010 and 100 in addition to the basic reflections from the body-centered tetragonal $ThCr_2Si_2$-type subcell. One may note a presence of the streak line at $^1/_2$ [$\bar{1}$10] distance parallel to the [001] direction in the [110] ED pattern (Figure 8b) similar to the one observed in the SC sample (see Figure 5b). Weak orthorhombic ($b/a = 1.060$) distortion was also often observed.

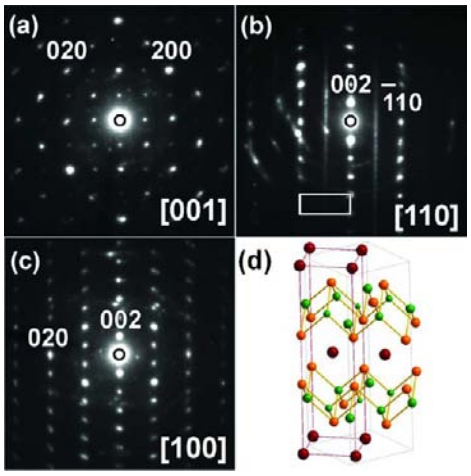

Figure 8. Electron diffraction patterns of non-SC $Rb_xFe_{2-y}Se_2$ (sample 2) taken along the (a) [001], (b) [110], and (c) [100] zone-axis directions. (d) Structural model for superstructure IV. The Rb, Fe, and Se atoms are indicated as red, green, and orange circles, respectively. The edges of the original $ThCr_2Si_2$ subcell are drawn in red color. The relative diameter of spheres represents the occupancy of the respective positions.

The appearance of the additional spots in the ED patterns for sample 2 might be associated with a new variant of Fe vacancy ordering, which was not observed for the SC sample. The search for such a variant was done using the program ISODISTORT.[45] Fe ordering was chosen as the only distortion parameter, and the search was conducted over all special k-points. It was shown that the observed reflection conditions may correspond to the superstructure with the space group *Pccm* derived by the irreducible representation X4− of the parent *I*4/*mmm* space group. The corresponding unit cell is based on the vectors $a_{IV} = a_s + b_s$, $b_{IV} = -a_s + b_s$, and $c_{IV} = c_s$, with the origin shift ($^1/_2$, 1, 0). The former 4*d* Fe positions of the original cell split under such transformation into 2*e*, 2*h*, 2*g*, and 2*f* positions of the supercell.

7. HRTEM Studies. HRTEM images along the [010] zone-axis direction are given in Figures 9−11. They confirm the presence of the partly disordered structure along the *c*-axis with various translations along the crystallographic planes in both

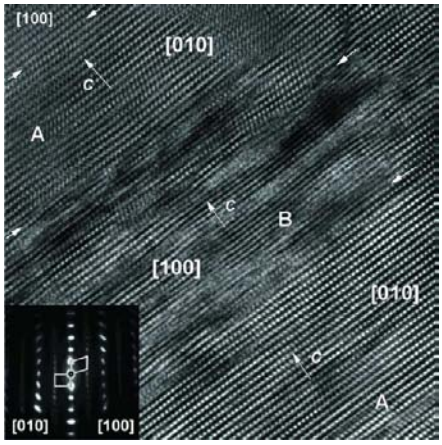

Figure 9. HRTEM image of a relatively large area of the non-SC $Rb_xFe_{2-y}Se_2$ sample. The microstructure combines different ordering patterns (A) and disordered regions (B).

dx.doi.org/10.1021/ic402710r | *Inorg. Chem.* 2013, 52, 14419−14427

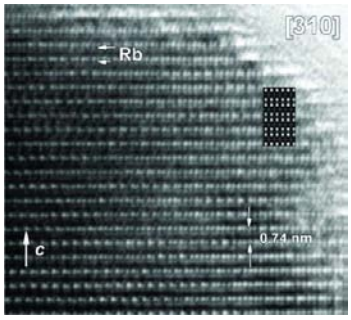

Figure 10. HRTEM image of the thin specimen of the SC sample 1. Image simulation based on the $I4/m$ model with cell parameters $a_I = b_I \approx 8.7$ Å, and $c_I \approx 14.5$ Å. The sample thickness of 6 nm and defocus of −30 nm were used for the pattern simulation.

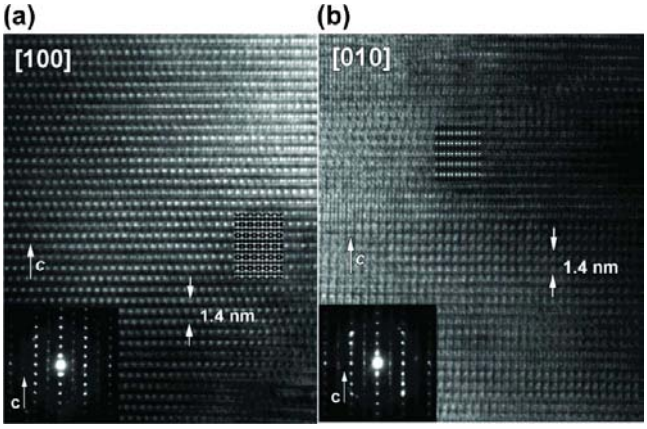

Figure 11. HRTEM images of the SC sample 1 in the (a) [100] and (b) [010] zone-axis directions. Image simulation based on the proposed *Ammm* model with cell parameters $a_{III} = b_{III} \approx 5.5$ Å, and $c_{III} \approx 14.5$ Å. The sample thickness of 13.2 nm and defocus of −65 nm were used for pattern simulation in the [100] zone, and the sample thickness of 6.6 nm and defocus of −20 nm were used for the pattern simulation in the [010] zone.

the superconducting and non-superconducting samples. The superconducting sample was found to be even more ordered in comparison to the non-superconducting one. Figure 9 shows the [100] HRTEM image of a relatively large area of the non-superconducting sample 2. The microstructure of this area is very inhomogeneous and combines different ordering patterns (A) and disordered regions (B).

Figure 10 shows the [310] HRTEM image of the superconducting sample 1. Note that the image characteristics strongly depend on the specimen thickness. At the thinnest edges of the crystal a well-defined 122-type layered structure is observed in agreement with the literature data.[10] Image simulation was carried out for the $I4/m$ structure (cell parameters $a_I = b_I \approx 8.7$ Å and $c_I \approx 14.5$ Å) with the Fe occupancy equal to 1 in the 16*i* sites and 0.15 in the 4*d* sites. The structural model that corresponds to superstructure I is given in Figure 5e. The pattern is the columns of square bright dots separated by dark stripes spaced by 0.74 nm. For this focus value the bright dots are correlated with the voids between Rb and Se positions. Rb atoms are represented by dark dots in the centers of the bright dots squares. The Fe atoms are imaged as hardly visible gray dots between the columns of the bright dots squares.

With the increase of the sample thickness the contrast might change probably due to the vacancy ordering within the bulk of the material. For the SC sample we observed two different variants of contrast in HRTEM images, which correspond to the diffraction patterns with two variants of additional spots rows (Figure 11). Image simulation based on the proposed *Ammm* model (cell parameters $a_{III} = b_{III} \approx 5.5$ Å and $c_{III} \approx 14.5$ Å) with a full occupancy of all Fe and Se sites and Rb occupancy equal to 0.3 in the 2*a* sites and 1 in the 2*c* sites was used. The structural model corresponds to superstructure III (Figure 6c). In the [010] zone-axis direction the picture represents a complex pattern of spots with different brightness grouped into small clusters spaced by 0.7 nm in the *c*-direction and by 0.55 nm in the *b*-direction. For the used sample thickness and defocus values the brightest dots are correlated with the voids between Rb atoms in the 2*a* and the 2*c* sites. In the [100] direction the pattern is imaged as a quasi-hexagonal net of bright spots corresponding to Rb atoms in the 2*c* positions. The simulated images reasonably match the experimental ones confirming the validity of the proposed structure model. This finding illustrates for the first time an experimental observation of the Rb ordering in the SC $Rb_xFe_{2-y}Se_2$ material.

IV. CONCLUSION

We have prepared single crystalline samples in the Rb−Fe−Se system and characterized them thoroughly by means of EDX, XRD, and magnetization and resistivity measurements. For the first time the superconducting and the non-superconducting $Rb_xFe_{2-y}Se_2$ materials with close composition were investigated in detail by TEM in order to understand the structural features that might be associated with the onset of superconductivity. The Rb−Fe−Se system reveals a rich variety of structural phenomena, which originate from the microinhomogeneity of the samples. Comparing the SC (T_C = 23 K) and non-SC samples, we have shown that the alternation of ordered and disordered regions on the sample surface and along the *c*-axis is characteristic for both types of materials and therefore does not necessarily represent a trigger of superconductivity. We have found that the SC material features a more complex superstructure pattern. In addition to the well-established $\sqrt{5} \times \sqrt{5}$ superstructure (space group $I4/m$), two other types of superstructures were observed for the SC material only. Altogether, they show a complex ordering pattern of iron and rubidium atoms, which cannot be rationalized using a single unit cell. For the non-SC sample we have observed another superstructure originating from the ordering of the iron atoms within the *ab*-plane. Moreover a monoclinic distortion leading to the space group $I2/m$ has been observed for the SC material. Such a distortion seems to be a prerequisite of the SC material and could be induced by an internal stress caused by the coexistence of several related phases within a single crystal. This internal stress manifesting in the monoclinic distortion may be one of the main ingredients for the observation of superconductivity in the Rb−Fe−Se system.

It is important to note that a part of the Fe vacancy ordered superstructures found in this study for the SC phase was previously observed for the non-SC $K_x(Fe,Co)_{2-y}Se_2$ sample.[13] The fact that a similar microstructure in the *ab*-plane was observed in both superconducting and non-superconducting samples with different alkali metals may indicate that the structural ordering does not significantly influence the onset of superconductivity. Therefore, only three structural features

dx.doi.org/10.1021/ic402710r | Inorg. Chem. 2013, 52, 14419−14427

remain that discriminate SC and non-SC materials of the $A_xFe_{2-y}Se_2$ family. These are the previously observed *ab*-plane compression leading to the sharp increase of the *c*/*a* ratio for the SC material as well as the monoclinic distortion and the alkali metal ordering established in this study.

AUTHOR INFORMATION

Corresponding Author

*E-mail: shev@inorg.chem.msu.ru.

Notes

The authors declare no competing financial interest.

ACKNOWLEDGMENTS

M.R. is grateful to A. Ovchinnikov for helpful discussions. The authors thank Dr. N. Khasanova and Dr. A. Garshev for XRD measurements and S. Pichl, G. Kreutzer, R. Müller, C. Malbrich, and K. Leger for technical support. Financial support by RFBR 12-03-91674-ERA_a, 12-03-01143 and 12-03-31717 is cordially acknowledged. Funding by Deutsche Forschungsgemeinschaft (DFG) is acknowledged under Projects WU595/3-1 (S.W.) and BE1749/13 and BU887/15-1 (B.B). This project was supported by Bundesministerium für Bildung und Forschung (BMBF) in the ERA.Net RUS program (Project 245 FeSuCo).

REFERENCES

(1) (a) Dagotto, E. *Rev. Mod. Phys.* **2013**, *85*, 849. (b) Shein, I. R.; Ivanovskii, A. L. *Solid State Commun.* **2011**, *151*, 671. (c) Ganguli, A. K.; Prakash, J. *Eur. J. Inorg. Chem.* **2011**, 3868.

(2) Mou, D. X.; Zhao, L.; Zhou, X. J. *Front. Phys.* **2011**, *6*, 410.

(3) Zavalij, P.; Bao, W.; Wang, X.; Ying, J.; Chen, X.; Wang, D.; He, J.; Wang, X.; Chen, G.; Hsieh, P. Y.; Huang, Q.; Green, M. *Phys. Rev. B: Condens. Matter Mater. Phys.* **2011**, *83*, 132509.

(4) Bacsa, J.; Ganin, A. Y.; Takabayashi, Y.; Christensen, K. E.; Prassides, K.; Rosseinsky, M. J.; Claridge, J. B. *Chem. Sci.* **2011**, *2* (6), 1054.

(5) Bao, W.; Huang, Q. Z.; Chen, G. F.; Wang, D. M.; He, J. B.; Qiu, Y. M. *Chin. Phys. Lett.* **2011**, *28* (8), No. 086104.

(6) Wang, M.; Wang, M.; Li, G.; Huang, Q.; Li, C.; Tan, G.; Zhang, C.; Cao, H.; Tian, W.; Zhao, Y.; Chen, Y.; Lu, X.; Sheng, B.; Luo, H.; Li, S.; Fang, M.; Zarestky, J.; Ratcliff, W.; Lumsden, M.; Lynn, J.; Dai, P. *Phys. Rev. B: Condens. Matter Mater. Phys.* **2011**, *84* (9), No. 094504.

(7) Ye, F.; Chi, S.; Bao, W.; Wang, X. F.; Ying, J. J.; Chen, X. H.; Wang, H. D.; Dong, C. H.; Fang, M. *Phys. Rev. Lett.* **2011**, *107* (13), 137003.

(8) Pomjakushin, V. Yu.; Pomjakushina, E. V.; Krzton-Maziopa, A.; Conder, K.; Shermadini, Z. *J. Phys.: Condens. Matter* **2011**, *23* (15), 156003.

(9) Pomjakushin, V. Yu.; Sheptyakov, D. V.; Pomjakushina, E. V.; Krzton-Maziopa, A.; Conder, K.; Chernyshov, D.; Svitlyk, V.; Shermadini, Z. *Phys. Rev. B: Condens. Matter Mater. Phys.* **2011**, *83* (14), 144410.

(10) Wang, Z.; Song, Y. J.; Shi, H. L.; Wang, Z. W.; Chen, Z.; Tian, H. F.; Chen, G. F.; Guo, J. G.; Yang, H. X.; Li, J. Q. *Phys. Rev. B: Condens. Matter Mater. Phys.* **2011**, *83* (14), 140505(R).

(11) Li, J. Q.; Song, Y. J.; Yang, H. X.; Wang, Z.; Shi, H. L.; Chen, G. F.; Wang, Z. W.; Chen, Z.; Tian, H. F. Cornell University Library archive no. arXiv:1104.5340, 2011.

(12) Song, Y. J.; Wang, Z.; Wang, Z. W.; Shi, H. L.; Chen, Z.; Tian, H. F.; Chen, G. F.; Yang, H. X.; Li, J. Q. *Europhys. Lett.* **2011**, *5* (3), 37007.

(13) Kazakov, S. M.; Abakumov, A. M.; Gonzalez, S.; Perez-Mato, J. M.; Ovchinnikov, A. V.; Roslova, M. V.; Boltalin, A. I.; Morozov, I. V.; Antipov, E. V.; Van Tendeloo, G. *Chem. Mater.* **2011**, *23*, 4311.

(14) Li, W.; Ding, H.; Deng, P.; Chang, K.; Song, C. L.; He, K.; Wang, L. L.; Ma, X. C.; Hu, J. P.; Chen, X.; Xue, Q. K. *Nat. Phys.* **2011**, *8*, 126.

(15) Cai, P.; Ye, C.; Ruan, W.; Zhou, X. D.; Wang, A. F; Zhang, M.; Chen, X. H.; Wang, Y. Y. *Phys. Rev. B: Condens. Matter Mater. Phys.* **2012**, *85*, 094512.

(16) Zhao, J.; Huibo, C.; Bourret-Courchesne, E.; Lee, D. H.; Birgeneau, R. J. Cornell University Library archive no. arXiv:1205.5992. 2012.

(17) Bao, W.; Li, G. N.; Huang, Q. Z.; Chen, G. F.; He, J. B.; Wang, D. M.; Green, M. A.; Qiu, Y. M.; Luo, J. L.; Wu, M. M. *Chin. Phys. Lett.* **2013**, *30*, No. 027402.

(18) Ricci, A.; Poccia, N.; Campi, G.; Joseph, B.; Arrighetti, G.; Barba, L.; Reynolds, M.; Burghammer, M.; Takeya, H.; Mizuguchi, Y.; Takano, Y.; Colapietro, M.; Saini, N. L.; Bianconi, A. *Phys. Rev. B: Condens. Matter Mater. Phys.* **2011**, *84*, No. 060511(R).

(19) Ricci, A.; Poccia, N.; Joseph, B.; Arrighetti, G.; Barba, L.; Plaisier, J.; Campi, G.; Mizuguchi, Y.; Takeya, H.; Takano, Y.; Saini, N. L.; Bianconi, A. *Supercond. Sci. Technol.* **2011**, *24*, No. 082002.

(20) Svitlyk, V.; Chernyshov, D.; Pomjakushina, E.; Krzton-Maziopa, A.; Conder, K.; Pomjakushin, V.; Dmitriev, V. *Inorg. Chem.* **2011**, *50*, 10703.

(21) Texier, Y.; Deisenhofer, J.; Tsurkan, V.; Loidl, A.; Isonov, D. S.; Friemel, G.; Bobroff, J. *Phys. Rev. Lett.* **2012**, *108*, 237002.

(22) Torchetti, D. A.; Fu, M.; Christensen, D. C.; Nelson, K. J.; Imai, T.; Lei, H. C.; Petrovic, C. *Phys. Rev. B: Condens. Matter Mater. Phys.* **2011**, *83*, 104508.

(23) Shermadini, Z.; Luetkens, H.; Khasanov, R.; Krzton-Maziopa, A.; Conder, K.; Pomjakushina, E. V.; Klauss, H. H.; Amato, A. *Phys. Rev. B: Condens. Matter Mater. Phys.* **2012**, *85*, 100501.

(24) Ryan, D. H.; Rowan-Weetaluktuk, W. N.; Cadogan, J. M.; Hu, R.; Straszheim, W. E.; Bud'ko, S. L.; Canfield, P. C. *Phys. Rev. B: Condens. Matter Mater. Phys.* **2011**, *83*, 104526.

(25) Ksenofontov, V.; Wortmann, G.; Medvedev, S. A.; Tsurkan, V.; Deisenhofer, J.; Loidl, A.; Felser, C. *Phys. Rev. B: Condens. Matter Mater. Phys.* **2011**, *84*, 180508(R).

(26) Speller, S. C.; Britton, T. B.; Hughes, G. M.; Krzton-Maziopa, A.; Pomjakushina, E.; Conder, K.; Boothroyd, A. T.; Grovenor, C. R. M. *Supercond. Sci. Technol.* **2012**, *25*, No. 084023.

(27) Landsgesell, S.; Abou-Ras, D.; Wolf, T.; Alber, D.; Prokeš, K. *Phys. Rev. B: Condens. Matter Mater. Phys.* **2012**, *86*, 224502.

(28) Bosak, A.; Svitlyk, V.; Krzton-Maziopa, A.; Pomjakushina, E.; Conder, K.; Pomjakushin, V.; Popov, A.; de Sanctis, D.; Chernyshov, D. Cornell University Library archive no. arXiv:1112.2569. 2011.

(29) (a) Pomjakushin, V. Yu.; Krzton-Maziopa, A.; Pomjakushina, E. V.; Conder, K.; Chernyshov, D.; Svitlyk, V.; Bosak, A. *J. Phys.: Condens. Matter.* **2012**, *24*, 435701. (b) Shoemaker, D. P.; Chung, D. Y.; Claus, H.; Francisco, M. C.; Avci, S.; Llobet, A.; Kanatzidis, M. G. *Phys. Rev. B: Condens. Matter Mater. Phys.* **2012**, *86*, 184511.

(30) Ding, X.; Fang, D.; Wang, Z.; Yang, H.; Liu, J.; Deng, Q.; Ma, G.; Meng, C.; Hu, Y.; Wen, H. H. *Nat. Commun.* **2013**, *4*, 1897.

(31) Tsurkan, V.; Deisenhofer, J.; Günther, A.; Krug von Nidda, H. A.; Widmann, S.; Loidl, A. *Phys. Rev. B: Condens. Matter Mater. Phys.* **2011**, *84*, 144520.

(32) Kanatzidis, M. G.; Pöttgen, R.; Jeitschko, W. *Angew. Chem., Int. Ed.* **2005**, *44*, 6996.

(33) *WinXPow*; STOE & Cie GmbH: Darmstadt, Germany, 2003

(34) Petricek, V.; Dusek, M.; Palatinus, L. *Jana2006. The crystallographic computing system*; Institute of Physics: Praha, Czech Republic, 2006.

(35) Klepp, K. O.; Sparlinek, W.; Boller, H. *J. Alloys Compd.* **1996**, *238*, 1.

(36) Xie, L.; Yin, Y. W.; Teng, M. L.; Su, T. S.; Li, X. G.; Li, J. Q. *Appl. Phys. Lett.* **2013**, *102*, 182601.

(37) Margadonna, S.; Takabayashi, Y.; McDonald, M. T.; Kasperkiewicz, K.; Mizuguchi, Y.; Takano, Y.; Fitch, A. N.; Suard, E.; Prassides, K. *Chem. Commun. (Cambridge, U. K.)* **2008**, 5607.

(38) Hsu, F. C.; Luo, J. Y.; The, K. W.; Chen, T. K.; Huang, T. W.; Wu, P. M.; Lee, Y. C.; Huang, Y. L.; Chu, Y. Y.; Yan, D. C.; Wu, M. K. *Proc. Natl. Acad. Sci. U. S. A.* **2008**, *105*, 14262.
(39) Shen, B.; Zeng, B.; Chen, G. F.; He, J. B.; Wang, D. M.; Yang, H.; Wen, H. H. *EPL* **2011**, *96*, 37010.
(40) Wang, D. M.; He, J. B.; Xia, T.-L.; Chen, G. F. *Phys. Rev. B: Condens. Matter Mater. Phys.* **2011**, *83*, 132502.
(41) Liu, R. H.; Luo, X. G.; Zhang, M.; Wang, A. F.; Ying, J. J.; Wang, X. F.; Yan, Y. J.; Xiang, Z. J.; Cheng, P.; Ye, G. J.; Li, Z. Y.; Chen, X. H. *EPL* **2011**, *94*, 27008.
(42) Mito, M.; Pitcher, M. J.; Crichton, W.; Garbarino, G.; Baker, P. J.; Blundell, S. J.; Adamson, P.; Parker, D. R.; Clarke, S. J. *J. Am. Chem. Soc.* **2009**, *131*, 2986.
(43) Wojdeł, J. C.; de Moreira, I. P. R.; Illas, F. *J. Am. Chem. Soc.* **2009**, *131*, 906.
(44) Wang, X. F.; Wu, T.; Wu, G.; Liu, R. H.; Chen, H.; Xie, Y. L.; Chen, X. H. *New J. Phys.* **2009**, *11*, No. 045003.
(45) Werthamer, N. R.; Helfand, E.; Hohenberg, P. C. *Phys. Rev.* **1966**, *147*, 295.
(46) Campbell, B. J.; Stokes, H. T.; Tanner, D. E.; Hatch, D. M. *J. Appl. Crystallogr.* **2006**, *39*, 607.